applied optics

Hybrid ray-tracing/Fourier optics method to analyze multilayer diffractive optical elements

Victor Laborde,[1,*] Jérôme Loicq,[1,2] Juriy Hastanin,[1] and Serge Habraken[1]

[1]Centre Spatial de Liege, Avenue du Pré-Aily, 4031 Angleur, Belgium
[2]Faculty of Aerospace Engineering, Delft University of Technology, Kluyverweg 1, 2629 HS Delft, The Netherlands
*Corresponding author: victor.laborde@uliege.be

Received 11 February 2022; revised 5 May 2022; accepted 5 May 2022; posted 9 May 2022; published 27 May 2022

The performance (paraxial phase delay) of conventional diffractive optical elements is generally analyzed using the analytical scalar theory of diffraction, based on thin-element approximation (TEA). However, the high thickness of multilayer diffractive optical elements (MLDOEs) means that TEA yields inaccurate results. To address this, we tested a method based on ray-tracing simulations in mid-wave and long-wave infrared wave bands and for multiple f-numbers, together with the effect of MLDOE phase delay on a collimated on-axis beam with an angular spectrum method. Thus, we accurately generate optical figures of merit (point spread function along the optical axis, Strehl ratio at the "best" focal plane, and chromatic focal shift) and, by using a finite-difference time-domain method as a reference solution, demonstrate it as a valuable tool to describe and quantify the longitudinal chromatic aberration of MLDOEs.

https://doi.org/10.1364/AO.456055

1. INTRODUCTION

Earth observation in the thermal infrared (IR) domain covers a wide range of applications, including security, land, and solid-Earth geophysics, health, and hazards monitoring [1,2]. Multispectral spaceborn instruments are particularly interesting, as they provide the high coverage required for most applications. We consider two IR wave bands, defined by the atmospheric IR windows: the mid-wave infrared (MWIR) from 3 to 5 μm and the long-wave infrared (LWIR) from 8 to 12 μm. The MWIR band is often shortened (4.4–5 μm) to avoid solar albedo contributions. Only a handful of optical materials are transmissive in both MWIR and LWIR, even though the relatively new chalcogenide family [3], composed of "soft" moldable materials, has enhanced the IR catalog. Generally speaking, refractive IR dual-band instruments are complex, expensive, and bulky, one reason being the large number of lenses needed to correct optical aberrations, especially chromatic and thermal defocus.

The most effective way to solve these defocus aberrations, in addition to the bulkiness issues, is to use diffractive lenses. When combined with refractive components (hybrid doublets), lenses correct most of the chromatic aberration and still remain compact. It should be noted that conventional monolayer diffractive lenses can operate in only a narrow spectral range, rendering them useless for dual-band applications. Since LWIR wavelengths are 2 times higher than MWIR wavelengths, the use of higher-order diffractive optical elements (DOEs) may provide a valuable alternative, with the first and second orders being used, respectively, in LWIR and MWIR. However, the addition of another working order for shorter wavelengths creates a discontinuity in the chromatic focal shift, rendering correction of the longitudinal chromatic aberration (LCA) difficult. This drawback can be overcome by using an extended dual-band diffractive solution, called a multilayer diffractive optical element (MLDOE). This optical component has been intensively studied since 1997 [4]. The most common approach used for modeling an MLDOE is analytical scalar diffraction theory (SDT). MLDOEs, composed of two harmonic diffractive layers [5,6], are recognized as one of the most promising diffractive optical components. In the context of SDT [7,8], it has been demonstrated that the diffraction efficiency of such MLDOEs can reach over 95% in the whole MWIR-LWIR bandwidth for on-axis incidence. In addition, a properly selected design can also ensure a high diffraction efficiency for off-axis incidence [9,10]. It is instructive to note that SDT involves the thin-element approximation (TEA), which becomes progressively inaccurate with increasing diffractive microstructure height [11,12]. In the case of MLDOEs, the typical heights of the grooves are 100 times higher than in conventional monolayer DOEs. Accordingly, rigorous electromagnetic numerical approaches such as the rigorous coupled-wave analysis have been used to model the effect of microstructure depth and incident angle on the diffraction efficiency of multilayer saw-tooth optical elements [13,14]. However, these rigorous approaches, far more accurate than SDT, are computationally intensive, especially in the case of three-dimensional design modeling. Recently, attractive approaches have involved geometric optics

approximations. These sit between analytic TEA and rigorous electromagnetic methods. For instance, the effective-area method has been proposed to perform accurate computations of diffraction efficiency for saw-tooth MLDOEs [15,16]. Using geometric optics approximations to describe an optical component's phase delay is also a method used by field tracing [17]. Field tracing often combines rigorous or approximate phase models with exact Fourier optics propagation tools to obtain the most efficient and reliable field description through complex optical systems.

In this paper, we use a scalar, ray-tracing based method (which we call our "ray model") instead of TEA to compute MLDOE phase delay. This approach is not new and was developed in [18] under the name "zone decomposition" modeling for the design of hybrid optical systems. It is further implemented in [19] and coupled with diffraction calculation to estimate the modulation transfer function of relief-type DOEs. We aim to examine the reliability and accuracy of the ray model compared with TEA in the case of MLDOEs. The latter predicts nearly perfect imaging performance [20], whereas the former heavily depends on refractive index variations and aspect ratios, due to Snell's law of refraction. Because neither of these scalar approaches is rigorous, an electromagnetic phase calculation is conducted using the finite-difference time-domain (FDTD) method. This provides a reference solution from which the accuracy of the ray model predictions can be assessed. The outputs of each of the three methods (TEA, ray model, and FDTD) are the MLDOE phase and amplitude patterns in the near field. Consequently, a Fourier optics propagator based on the angular spectrum method is used to generate optical fields and evaluation metrics in the far field, at the detector plane (similarly to [19]). Both MWIR and LWIR wave bands are investigated.

Fourier optics provides an exact free-space propagation method that generates performance outputs based on a phase mask input (Section 2). Three input phase models are studied, respectively, based on the TEA (Section 3), the ray model (Section 4), and FDTD (Section 4). Approximate scalar models (TEA and ray model) and FDTD are compared in Section 5, providing an analysis of the beam shape along the optical axis and the imaging performance at the focal plane. Various wavelengths, materials, and f-numbers ($F/\#$) are considered.

2. FOURIER-BASED SIMULATION PROCESS

A. Wave Propagation Using Fourier Optics

Analysis using Fourier transform formalism is a powerful optical modeling tool introduced and popularized widely by Goodman [21]. It provides a straightforward method for evaluating, in any point in space, the properties (phase and amplitude) of a monochromatic electromagnetic wave, propagating in a free-space medium (linear, homogeneous, non-magnetic, free of electric charge and current). Under such assumptions, and far from the medium's boundaries, Maxwell's coupled-wave equations simplify into a single complex equation called the Helmholtz equation:

$$(\nabla^2 + k^2)U(\mathbf{r}) = 0, \tag{1}$$

where $U(\mathbf{r})$ is the exponential notation (phasor) of the complex amplitude distribution of the optical wave $u(\mathbf{r}, t)$; $\mathbf{r}$ is the vector position; t is time; and k is the wavenumber, defined as

$$k = 2\pi n\frac{\nu}{c} = \frac{2\pi}{\lambda}, \tag{2}$$

where λ is the wavelength in the dielectric free-space medium. The complex field phasor $U(P)$ expression can be retrieved by applying the Fourier transform for two parallel planes $z = 0$ and $z > 0$ and using Eq. (1) (demonstrated in more detail in [21]). This provides a powerful tool for accurately simulating optical wave propagation, commonly referred to as the angular spectrum method:

$$\begin{cases} U(x, y; z) = \mathcal{F}^{-1}\{\mathcal{F}\{U(x, y; 0)\}H_z(f_x, f_y)\} \\ H_z(f_x, f_y) = \mathcal{F}\{h_z(x, y)\} = \exp\left[ikz\sqrt{1 - (\lambda f_x)^2 - (\lambda f_y)^2}\right], \end{cases} \tag{3}$$

where (f_x, f_y) are the spatial frequencies of the field, H_z is the transfer function of the wave propagation phenomenon, and h_z is the impulse response of the system. Note that, since the angular spectrum method is constrained by free-space assumptions, it cannot be employed to compute the optical field propagation through an MLDOE. Therefore, Fourier optics is bounded to propagate a complex field, computed after the MLDOE, onto a target plane. Since the angular spectrum is a scalar method, it is limited to fields that do not contain components propagating at high numerical apertures (NAs) (e.g., angles greater than NA = 0.6). This is ensured by using the band-limited angular spectrum method developed in [22] (i.e., there is no aliasing due to high-frequency components).

B. Simulation and Comparison Process

This section describes the main simulation steps involved in our rationale to compare the TEA and ray models. The simulation and comparison process is shown in Fig. 1.

As indicated in Fig. 1, the optical effect of an MLDOE is described by a scalar complex phasor $U(x, y; 0) = A(x, y)\exp[i\Phi(x, y)]$ in both the TEA and ray models, considering an on-axis collimated monochromatic source. In contrast, FDTD provides an exact electromagnetic vectorial description of the MLDOE effects, encompassed in the electrical field $\mathbf{E} = (E_x, E_y)$. The calculations of these initial fields are detailed in Sections 3.A and 3.B. The resulting wavefront is propagated, using the angular spectrum of plane waves, to the focal plane, where the image quality of the MLDOE can be retrieved. The Strehl ratio and the LCA, also known as chromatic focal shift, provide a way to assess the optical quality. These evaluation metrics are computed in MWIR and LWIR for various $F/\#$. The "best" focal plane, *a priori* unknown, is defined in this paper as the plane $z > 0$ that provides the highest Strehl ratio. Consequently, it may differ from the expected analytic focal plane, whose expression is the same for standard DOEs and MLDOEs [20]:

$$f_j(\lambda) = D\frac{F/\#}{j\lambda}, \tag{4}$$

where j is the diffractive order ($j = 1$ is considered in this paper).

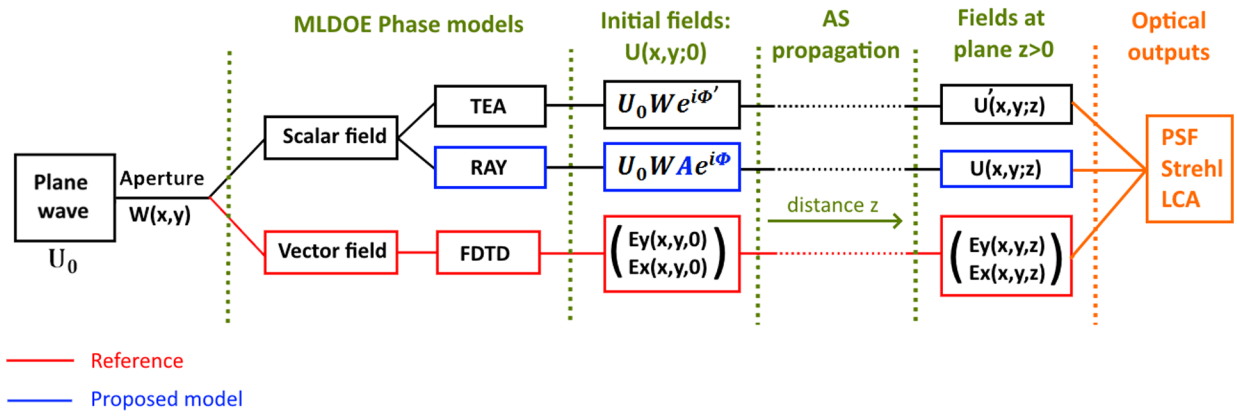

Fig. 1. Diagram showing the numerical processes involved in this paper, in order to compare the TEA and the ray model, using FDTD as reference.

3. MLDOE TEA DESIGN AND PHASE MODEL

This section derives the analytical phase model based on TEA, which is the most widely adopted model for the design of DOEs.

A. TEA Phase Model

An MLDOE is composed of two harmonic diffractive optical elements (HDOEs) [5,6] (Fig. 2), joined together by an optical material or separated by air. These HDOEs are made of different materials, and their groove heights are designed to provide constructive interference for two distinct wavelengths, called "design wavelengths" and denoted λ_1 and λ_2. In this paper, the selected design wavelengths are $\lambda_1 = 4.7\ \mu m$ and $\lambda_2 = 10.4\ \mu m$, based on a wavelength selection method [8] applied in both MWIR and LWIR. Both layers are aligned and have the same groove periods (i.e., the same number of diffractive zones). The TEA involves paraxial rays that travel through the component parallel to the optical axis, with no deviation. This leads to an analytical expression of optical path lengths (OPLs) and phase delay for each layer.

Figure 2 shows the geometric framework for the study of OPLs inside a MLDOE. The TEA implies a paraxial incident beam. The shape of layer $i = 1, 2$ along the optical axis z at radius r is described by $z_i(r)$; H_i is the maximal height of the profile; $f(\lambda)$ is the focal distance of the MLDOE at wavelength λ; and m is the diffractive zone being considered, starting at radius r_m and finishing at r_{m+1}. Each layer i is made of a distinct material with refractive index $n_i(\lambda)$, and the gap is filled with a material $n_g(\lambda)$. Interference between each zone is constructive at the focal plane.

The optical path differences for both DOEs 1 and 2 of the MLDOE layout can be calculated using the analytical equation [20]:

$$\Phi_{\mathrm{TEA}}(r,\lambda) = \frac{2\pi}{\lambda}\left[-H_1(n_1 - n_g) - H_2(n_2 - n_g)\right]\left(m - \frac{r^2}{r_1^2}\right). \tag{5}$$

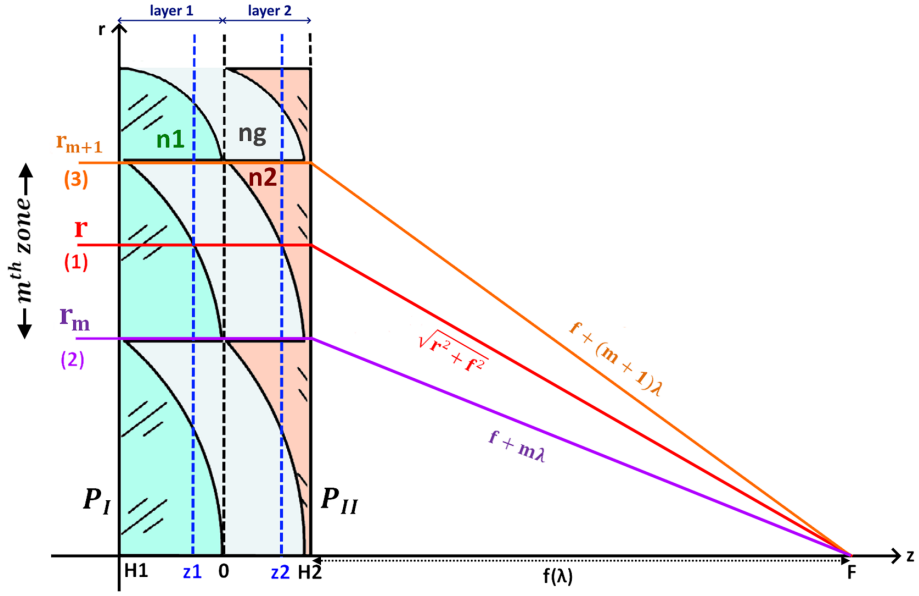

Fig. 2. Extended model of DOE to MLDOE.

In this equation, $\Phi_{\mathrm{TEA}}(r, \lambda)$ is the total phase delay under normal incidence. The layer heights H_1 and H_2 can be straightforwardly evaluated from Eq. (5) under the condition of constructive interference [20], for the first diffractive order and the two selected design wavelengths λ_1 and λ_2:

$$\begin{cases} H_1 = \frac{\lambda_2 A(\lambda_1) - \lambda_1 A(\lambda_2)}{B(\lambda_1)A(\lambda_2) - B(\lambda_2)A(\lambda_1)} \\ H_2 = \frac{\lambda_1 B(\lambda_2) - \lambda_2 B(\lambda_1)}{B(\lambda_1)A(\lambda_2) - B(\lambda_2)A(\lambda_1)} \end{cases}, \tag{6}$$

where $A(\lambda) = n_2(\lambda) - n_g(\lambda)$ and $B(\lambda) = n_1(\lambda) - n_g(\lambda)$. As seen in Eq. (5), the shape of each zone is parabolic due to the converging requirement in the MLDOE design. The complex scalar field phasor associated with the TEA model, expressed in the MLDOE near field at wavelength λ, is

$$U(x, y; \lambda) = \exp\left[i\Phi_{\mathrm{TEA}}(x, y; \lambda)\right]. \tag{7}$$

The amplitude is constant over the aperture. Finally, using the Pythagorean theorem in Fig. 2, the zone radius is given by

$$r_m^2 = 2mf\lambda_d + (m\lambda_d)^2 \simeq 2mf\lambda_d. \tag{8}$$

This standard definition of the period and radii of diffractive zones [Eq. (8)] is similar for MLDOEs and classical monolayer DOEs. In the following, the mth zone period T_m is defined as $T_m = r_{m+1} - r_m$, the ring width. The aspect ratio ($\mathcal{R}$) of the mth zone is, therefore, introduced:

$$\mathcal{R} = \max(H_1, H_2)/T_m. \tag{9}$$

B. TEA Validity: Numerical Comparison

In this section, the TEA boundaries are derived based on the study of MLDOE thicknesses (design based on Section 3). According to [12], the TEA remains valid when $\mathcal{R}$ [Eq. (9)] is less than 1/6. As seen in the previous section, this ratio is influenced by the material combination, the choice of design wavelengths, and the optical parameters $F/\#$ and diameter D. As an example, in this section, we fix the number of zones $N = 10$ and the aperture diameter $D = 10$ mm, keeping in mind manufacturability concerns.

We check the validity of the TEA (Fig. 3) in the worst-case scenarios by considering the lowest zone period and the thickest layer. This is done for various $F/\#$ and considering all possible MLDOE material combinations. In our study, each layer (as well as the gap) can consist of 12 potential IR materials: Ge, ZnS, ZnSe, GaAs, AgCl, CdTe, and six chalcogenide materials, from IRG22 to IRG27. We, therefore, define an "MLDOE combination" as a triplet of material (m_1, m_g, m_2). The denominations "two-layer DOE" and "three-layer DOE" are employed when the gap material m_g is, respectively, filled by air or by another IR material.

Figure 3 displays the aspect ratios obtained for each MLDOE combination and $F/\#$. Because changing any material in a combination can lead to very different aspect ratios, the latter are sorted by thickness in Fig. 3, where the cumulative percentage of MLDOE combinations is considered. This is the number of MLDOE combinations (in %) that display at most a specific aspect ratio for a given $F/\#$.

An air gap is imposed in Fig. 3(a). Only combinations with total height lower than 1 mm are depicted in Fig. 3, for a total of 253 combinations. Figure 3(a) shows that the TEA validity requirement is fulfilled for at most only 15% of two-layer DOEs, with a minimal f-number of 37. This degrades to 5% in Figs. 3(b) for three-layer DOEs.

The result is that the TEA model requirement is never satisfied, except for extremely high $F/\#$. Thereby, the period size

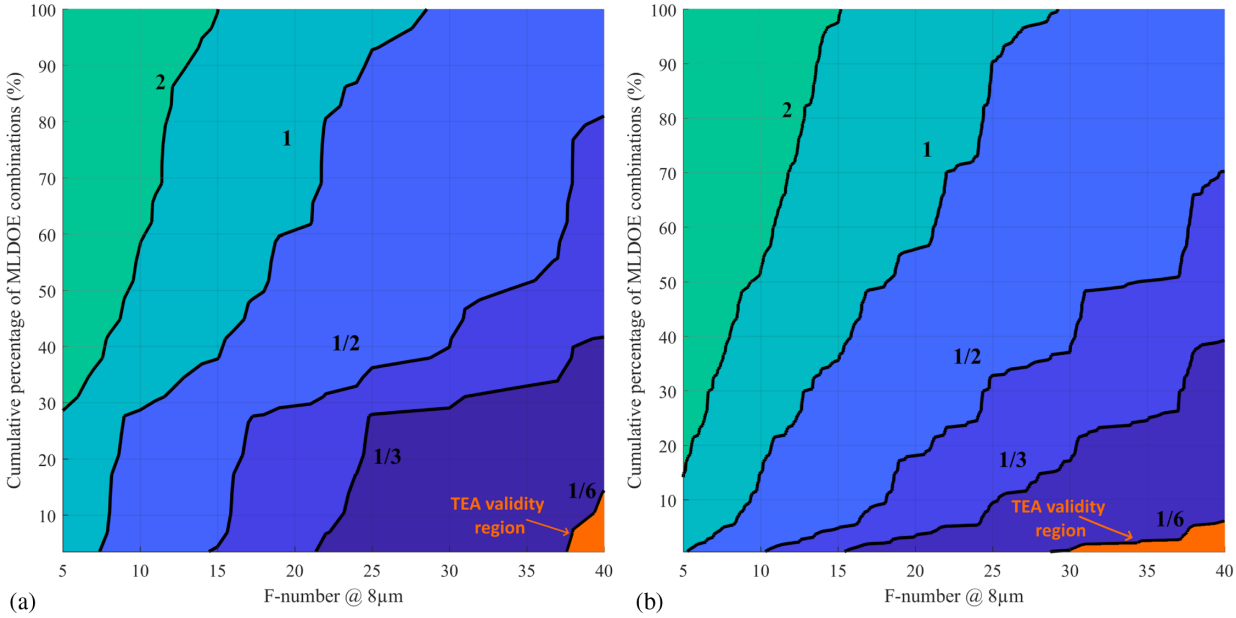

Fig. 3. MLDOE aspect ratios $\mathcal{R}$ [Eq. (9)] in function of the cumulative percentage of MLDOE combinations, for various $F/\#$. The combinations have been sorted from the thinnest ($\mathcal{R} < 1/6$) to the thickest ($\mathcal{R} > 2$) for all $F/\#$ between 5 and 40. (a) Two-layer DOE (air gap). b) Three-layer DOE (filled gap). The aperture diameter is fixed to $D = 9.6$ mm, and the design wavelengths are $\lambda_1 = 4.7$ µm and $\lambda_2 = 10.4$ µm. The worst case is considered: thickest layer and lowest zone period. Only material combinations with a total height <1 mm are kept and displayed, to keep a relatively thin element. The orange region shows the validity of the TEA model [12].

of MLDOEs and monolayer DOEs is the same [Eq. (8)], but MLDOEs are 10 to 100 times thicker than DOEs. For instance, considering a monolayer DOE, we analyze the TEA model's validity in the worst possible case: the lowest refractive index material, AgCl ($n \simeq 2$), and an f-number of 5 at $\lambda = 8\,\mu$m:

$$\mathcal{R}_{\mathcal{DOE}} = \frac{H}{T_{\min}} = \frac{\lambda}{(n-1)\,T_{\min}} \simeq 1/10 < 1/6. \tag{10}$$

Considering the validity region in Fig. 3, this numerical application proves that the TEA model, while accurate in the case of monolayer DOEs, is not suited for the study of MLDOEs.

For the rest of this paper, the design wavelengths are fixed to $\lambda_1 = 4.7\,\mu$m and $\lambda_2 = 10.4\,\mu$m. Two MLDOE combinations, arbitrary selected, will be considered for the comparison of ray and TEA models: a ZnS-air-Ge MLDOE and a ZnS-air-IRG25 MLDOE. The former combination has the lowest thickness among "air-gap combinations" and has already been studied in [20]. The ZnS-air-IRG25 combination is chosen to replace the expensive and hard Ge layer by a "softer" chalcogenide material, increasing the potential for manufacturability.

4. ALTERNATIVE PHASE MODELS: RAY MODEL AND FDTD

In this section, two alternatives to TEA are described. Our ray model, inspired by [18,19], examined in this paper is a scalar model based on the calculation of OPL using ray-tracing. FDTD is an electromagnetic calculation providing exact vectorial fields and serves as a reference solution for the comparison of the ray and TEA models.

A. Ray Model

As shown in Section 3, TEA is not suitable for describing MLDOE behavior except for very high $F/\#$. The examined ray model still belongs to SDT but introduces a deviation of the rays at each interface according to Snell's law of refraction. The assumption, used by the TEA, of rays traveling parallel to the optical axis is removed in the ray model. Therefore, OPLs are longer in the ray model, and their lengths strongly depend on the zone shape and aspect ratio, as well as on the transition from one material to another. Optical effects such as total internal reflection may appear for high aspect ratios/high index variations and are taken into account in the ray model.

The effect of an MLDOE on a plane wave is obtained in the near field through the calculation of a phase mask. The latter is computed following Eq. (11):

$$\Phi_{\text{ray}} = \frac{2\pi}{\lambda}\text{OPL} = \frac{2\pi}{\lambda}\sum_{i=1}^{3} n_{i;i+1}\text{OPL}_{i;i+1}, \tag{11}$$

where i is an optical interface of the MLDOE, numbered between 1 and 3, $n_{i;i+1}$ and $\text{OPL}_{i;i+1}$ are, respectively, the refractive index and the OPL between interface i and $i+1$. The latter is obtained using a ray-tracing engine (the professional modeling and ray-tracing software ASAP NextGen [23]).

Fundamentally, the ray model differs from the TEA model only by computation of the OPL. The complex scalar field phasor associated with the ray model is expressed in the near field of an MLDOE by [19]

$$U(x, y, \lambda) = A_{\text{ray}}(x, y)\exp\left[i\Phi_{\text{ray}}(x, y, \lambda)\right]. \tag{12}$$

It is interesting to notice that the TEA model is able, by design, to optimize the zone heights and OPLs to obtain the maximum performance at the focal plane regardless of the selected materials and aspect ratios (see Section 5). In contrast, the ray model is based on refraction at the interfaces and will provide phase masks that heavily depend on the material choice and aspect ratio. Thereby, the selection of materials and $F/\#$ will not only impact the focal length and the diffractive zone thickness, but also the optical performance at the focal plane.

B. FDTD Phase Simulation

Both TEA and ray models are scalar approximations; therefore, a third phase model is used as reference in this paper, computed with the vectorial FDTD method. This rigorous electromagnetic calculation method will serve as a reference solution to establish the accuracy of the ray model.

FDTD wave simulation is performed using OptiFDTD software [24]. Starting from a plane wave, a complex electric field is propagated numerically through the MLDOE. Only the E_x and E_y components are considered, with the E_z component being negligible, as it is along the propagation direction. The circular symmetry of the problem is used to reduce the sampling effort needed. The most adequate sampling is studied in the worst-case scenario: lowest F/# (F/10) and wavelength ($\lambda = 4.4\,\mu$m). Figure 4 shows the sampling converging curve,

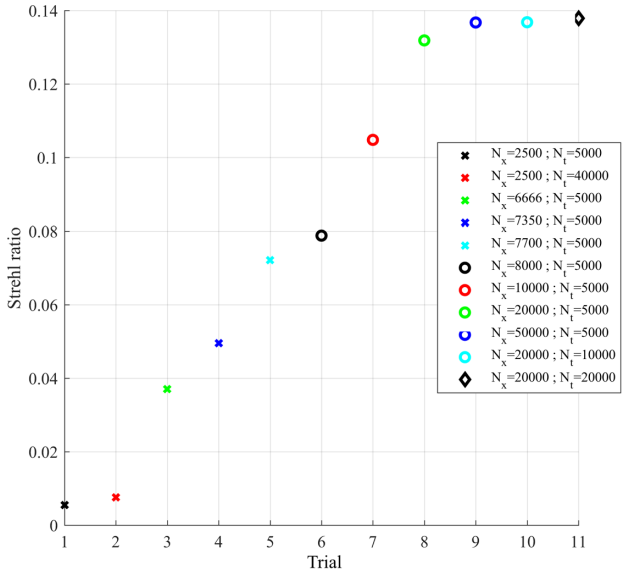

Fig. 4. FDTD sampling convergence curve. The metric associated with each sampling is the Strehl ratio, computed at the "best" focal plane. The sampling along the optical axis (N_z, δ_z), as well as the radial and time sampling steps δ_x and δ_t, are automatically computed by the OptiFDTD software. N_x is the number of samples in the radial dimension (perpendicular to wave propagation direction z), and N_t is the number of time steps.

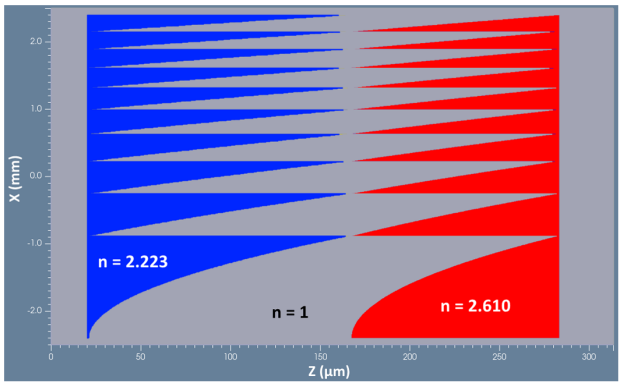

Fig. 5. Two-dimensional FDTD layout of a ZnS–IRG25 F/15 MLDOE. The source and the detector, respectively, lies in the planes $z = 0$ μm and $z = 300$ μm. The blue and red layouts represent the two HDOE layers, separated by an air gap.

obtained by computing the Strehl ratio at the focal plane, for each sampling.

The results of this numerical investigation (Fig. 4) confirm that the chosen metric converges for the sampling $N_x = 20{,}000$ and $N_t = 5000$, which is defined in the worst-case scenario. The resulting vectorial optical field obtained in the MLDOE near field is $E(x, y) = [E_x(x, y); E_y(x, y)]$. The E_x and E_y components are obtained, respectively, through separate transverse magnetic and transverse electric polarization simulations; therefore, they are not coupled. These two components can be propagated using the angular spectrum, and incoherently summed to obtain the point spread function (PSF), modulation transfer function, and Strehl ratio at the target plane, meaning that the simulation is done for unpolarized light.

Finally, the two-dimensional FDTD layout of one of the selected MLDOEs (ZnS-air-IRG25) is shown in Fig. 5.

The MLDOE layout of Fig. 5 was obtained by superposing parabola pieces made of the specified materials.

5. RESULTS

In this section, optical figures of merit (PSF, Strehl ratio, and LCA) are obtained based on the simulation process described in Fig. 1. Using these metrics, both the TEA and ray model are compared to FDTD. Two MLDOEs are considered: ZnS-air-Ge and ZnS-air-IRG25. The aperture diameter is fixed at $D = 9.6$ mm (Section 3).

A. Results Along the Optical Axis: PSF Comparison

We compare the irradiance along the optical axis, predicted by each of the three models (TEA, ray, and FDTD). We recall that, starting from an initial field at plane $z = 0$ (scalar or vectorial), the angular spectrum method allows us to accurately predict the resulting field at any parallel plane $z > 0$ in the context of free-space propagation. We propagate the fields to multiple planes z, and for each, we compute the PSF for all three models. FDTD vectorial field irradiances are incoherently added to provide a total irradiance output for each plane. Because we are comparing the wave propagation predicted by the two scalar models, we use a single setup: $\lambda = 8$ μm and $F/\# = 15$, giving an analytic focal length $f = F/\#D = 144$ mm. The "best" focal in this paper is obtained in the sense of the Strehl ratio, computed at each propagation plane.

Figure 6 displays the distribution of energy along the optical axis for the three models, for the ZnS-air-Ge MLDOE. The TEA model predicts diffraction-limited optical performance at the focal plane (Strehl ratio of 0.98), and the latter coincides with the analytical focal length value. This result is not in accordance with the prediction of the ray and FDTD models. In fact, both models predict that only a central portion of the MLDOE actually contributes to the focus energy. A secondary ring of light, coming from the "intermediate zones" also tends to converge, but to a further focal point, creating important stray light. Finally, both the ray and FDTD models predict a different "best" focal plane (around $z = 111$ mm) and different Strehl ratio values. The ray model is an approximate model, giving more pessimistic Strehl ratio values than FDTD (0.11 for the ray model and 0.24 for FDTD) for this design and f-number. Note that the number of zones contributing to the focus energy is higher for FDTD, explaining the lower peak irradiance value and, thus, the lower Strehl ratio for the ray model. A one-dimensional cut of the logarithm of the PSF at the best focal plane (yellow line) is displayed in Fig. 11(a) of Appendix A. The TEA model provides a diffraction-limited Airy pattern, while the other models predict a very different PSF shape. The secondary light ring visible in Figs. 6(b) and 6(c) clearly appears in Fig. 11(a), with an irradiance level of $10^{-1.5}$ Wm^{-2}. The ray model accurately predicts the existence of this secondary ring but, as mentioned above, underestimates the peak irradiance value compared with FDTD (and overestimates the secondary ring irradiance).

Figure 7 displays the same optical metric as Fig. 6: the variation of PSF along the optical axis, but for the ZnS-air-IRG25 MLDOE. As stated in the ray model description (Section 4), the TEA model generates the same diffraction-limited performance when the Ge layer is replaced by IRG25 [Fig. 7(a)]. The focal length remains equal to the analytical one: $f = 144$ mm. In contrast, the ray model and FDTD generate a similar beam shape in Fig. 7, with a thinner outer light ring. FDTD and ray models both predict the location of the best focal plane at $z = 86$ mm. Once again, the ray model is pessimistic with a Strehl ratio value of 0.11 against 0.18 for the FDTD. Figure 11(b) in Appendix A again shows the difference in PSF energy distribution between the TEA and the other two models.

The results of this section highlight the accuracy of the ray model over the TEA model. The former, even if less precise than FDTD, is able to retrieve the shape of the irradiance pattern at the focal point and along the optical axis, and to provide realistic estimates of irradiance peak value, Strehl ratio, and focal length. It is worth noting that changing the material of one or more layers has a strong impact on the optical performance, beam shape, and focal length.

B. Results at the Detector Plane: Strehl Ratio and LCA

In this section, we compare the TEA and ray model by using both the Strehl ratio and the chromatic focal shift as optical performance metrics. Multiple wavelengths in the MWIR and LWIR bandwidths and multiple $F/\#$ are studied for both ZnS-air-Ge and ZnS-air-IRG25 MLDOE combinations.

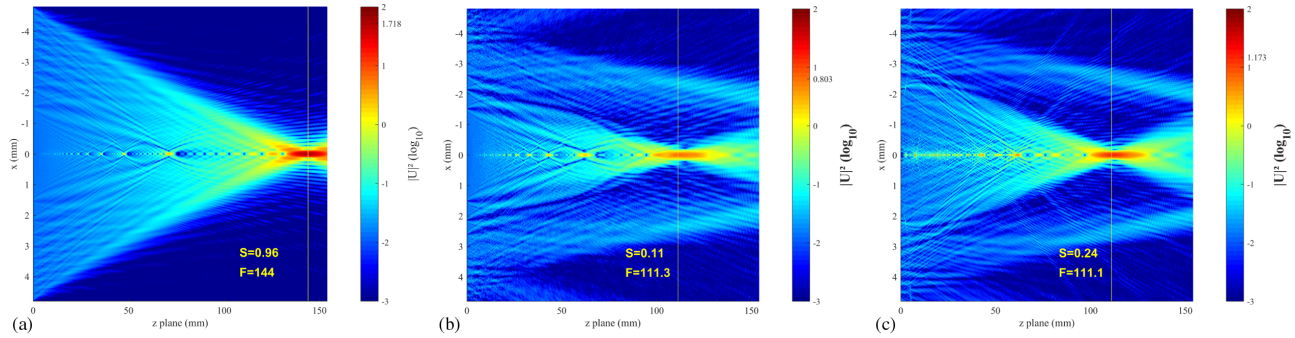

Fig. 6. PSF along the optical axis for a ZnS–Ge F/15 MLDOE considering: (a) the TEA model, (b) our ray model, and (c) FDTD. The initial plane is in $z = 0$ mm, just after the MLDOE component. The maximum irradiance value, obtained at the focal plane, is displayed in the color bar. The vertical yellow line shows the simulated "best" focal plane, whose value F as well as the associated Strehl ratio S are indicated in red. The predictions of the TEA model are too optimistic, in contrast to the ray model and FDTD.

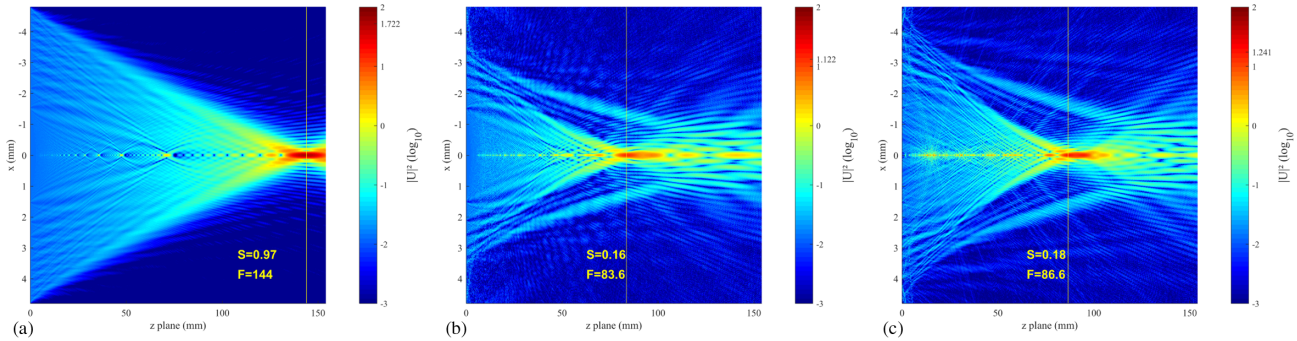

Fig. 7. PSF along the optical axis for a ZnS–IRG25 F/15 MLDOE considering: (a) the TEA model, (b) our ray model, and (c) FDTD. The initial plane is in $z = 0$ mm, just after the MLDOE component. The vertical yellow line shows the simulated "best" focal plane, whose value F as well as the associated Strehl ratio S are indicated in red. The maximum irradiance value, obtained at the focal plane, is displayed in the color bar. The predictions of the TEA model are too optimistic, again. In addition, these predictions are not impacted by the change of the Ge layer to an IRG25 layer. In contrast, this change has modified the predicted PSF, Strehl ratio, focal length, and beam shape in the case of the ray model and FDTD.

We recall that the chromatic focal shift (also known as LCA) is a major figure of merit for diffractive optics. Thereby, diffractive lenses mainly serve to provide efficient achromatic hybrid solutions when combined with refractive lenses, so the accurate knowledge of their LCA is of prime importance. The LCA is, therefore, associated with the design performance, while the Strehl ratio gives a direct optical performance metric.

Figure 8 shows the evolution of the IR Strehl ratio with the $F/\#$ for the three considered models (TEA, ray, and FDTD). The IR Strehl ratio Strehl_I is defined as

$$\text{Strehl}_I(F/\#) = \text{mean}_\lambda[\text{Strehl}(\lambda, F/\#)], \tag{13}$$

where the wavelength λ is in the range 4.4–12 μm.

As shown by the black flat curve of Fig. 8, the TEA model predicts a near-perfect IR Strehl ratio regardless of the materials and $F/\#$. However, looking at the ray model (red curve) and FDTD model (blue curve), we can infer more realistic behavior for both MLDOE designs: Increasing the $F/\#$ lowers the aspect ratio; thus, more light is likely to be collected at the focal plane. Likewise, less stray light will be generated by the MLDOE, resulting in an increase in the Strehl ratio. As seen in Fig. 3, decreasing the aspect ratio makes the TEA progressively more valid, providing asymptotic behavior as displayed in Fig. 8.

As previously noted in Figs. 6 and 7, for both MLDOE designs, on average for all wavelengths, the ray model gives more pessimistic results than FDTD, which, as will be discussed in Section 6, is an acceptable result. Nevertheless, the accuracy of the ray model remains inferior to the FDTD (which will be quantified in Section 5.C).

Figure 9 shows the evolution of the LCA with the wavelength for the ZnS-air-Ge MLDOE and various $F/\#$. The LCA is defined in this paper as $\text{LCA}(\lambda) = f(\lambda) - f(\lambda = 12\ \mu\text{m})$. A similar graph can be found in Appendix A for the ZnS-air-IRG25 MLDOE.

Figure 9 confirms that the TEA model (black curve) is perfectly in agreement with the diffractive lens focal law [Eq. (4), black diamond curve] for all $F/\#$. Both the FDTD and ray model (blue and red curve) are in good agreement for all $F/\#$, wavelength, and material combinations (see Fig. 10 in Appendix A). However, they disagree with the analytical expression [Eq. (4)] and with the TEA model.

C. Accuracy of the Ray Model

In this section, the accuracy of the ray model (its divergence from the FDTD model) is computed using the root mean square error (RMSE), presented in Table 1.

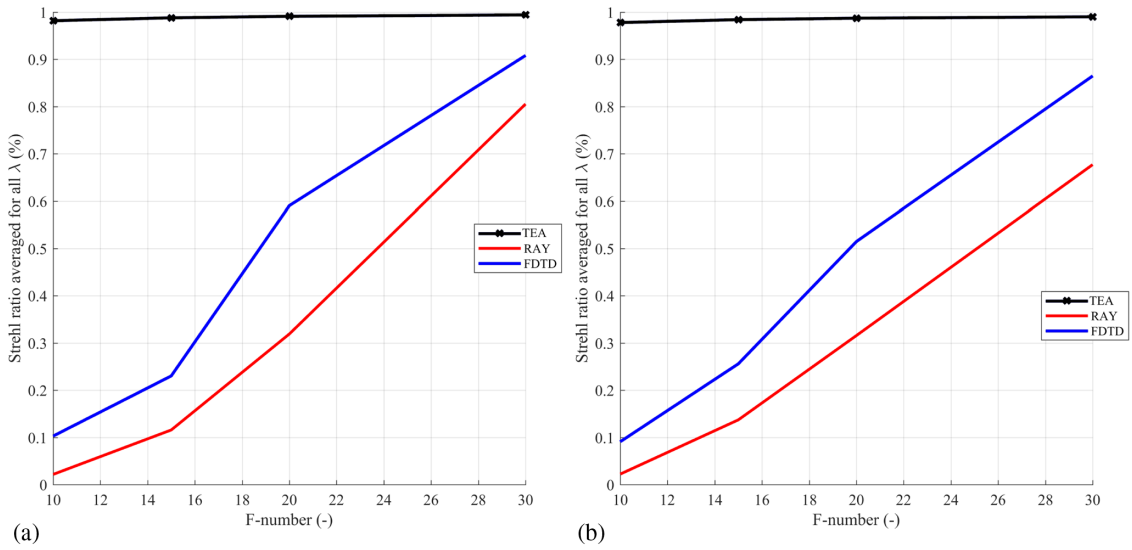

Fig. 8. Infrared Strehl ratio at the best focus for multiple $F/\#$. The TEA model, ray model, and FDTD are, respectively, displayed in black, red, and blue. Each point results from the wavelength averaged Strehl ratio in the 4.4–12 μm bandwidth. (a) ZnS-air-IRG25 MLDOE. (b) ZnS-air-Ge MLDOE.

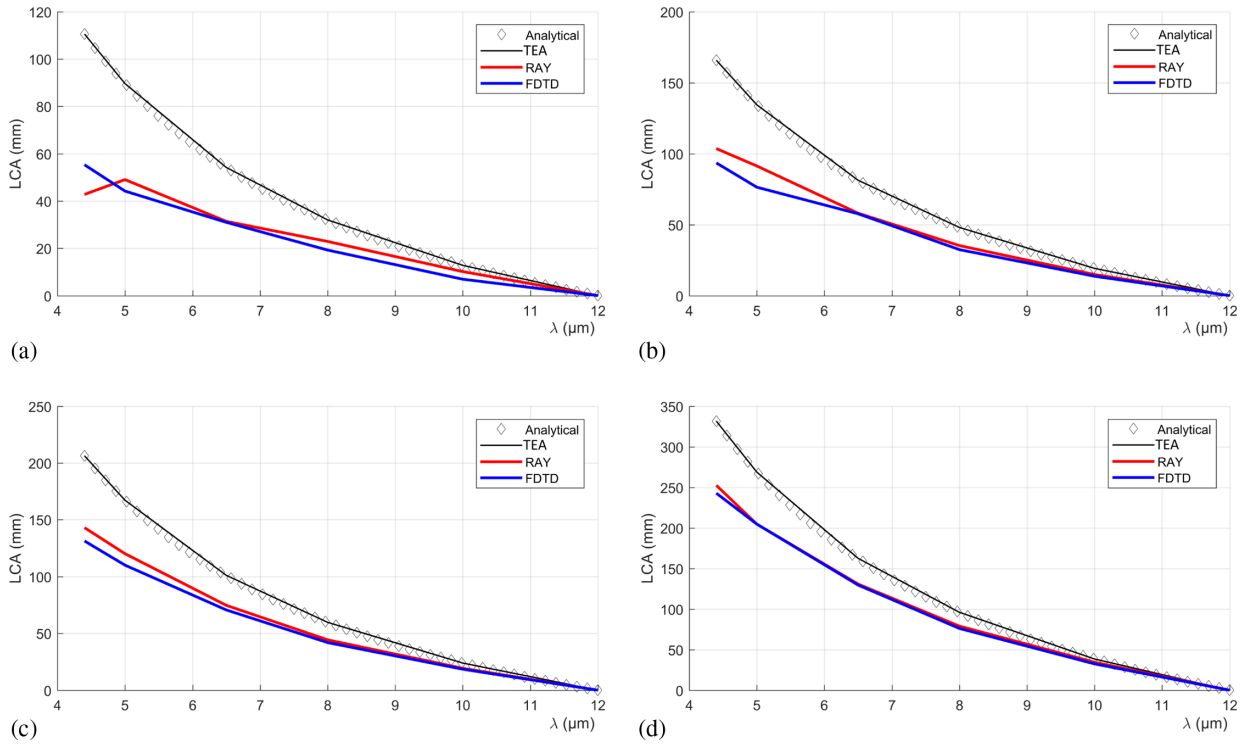

Fig. 9. LCA for a ZnS-air-Ge MLDOE for various $F/\#$: (a) F/10, (b) F/15, (c) F/20, and (d) F/30. The "best" focal plane is defined as the plane $z > 0$ with highest Strehl ratio. The TEA model, ray model, and FDTD are, respectively, displayed in black, red, and blue. The analytical LCA is displayed with black diamonds [Eq. (4)]. FDTD is the reference curve.

The RMSE metric describes the standard deviation of the residuals (the averaged distance between the FDTD model predictions and the ray model predictions). In the case of the LCA, the RMSE value (given in millimeters) must be compared to the LCA maximum extent (for the FDTD model) to be interpreted. The IR Strehl ratio RMSE is ∼15% for both designs, meaning that the ray model is not able to give accurate values of image quality. Nonetheless, it provides a good IR Strehl ratio tendency, especially when compared with the TEA model.

The LCA is well predicted by the ray model, with an RMSE between 4 and 8 mm. In the worst case [F/10 ZnS-air-IRG25 MLDOE, Fig. 10(a)], the LCA extent is 40 mm with RMSE $\simeq$ 6 mm (Table 1), leading to a worst-case relative RMSE of 15%. This value decreases to less than 10% for higher f-numbers, regardless of the design. The ray model worst-case

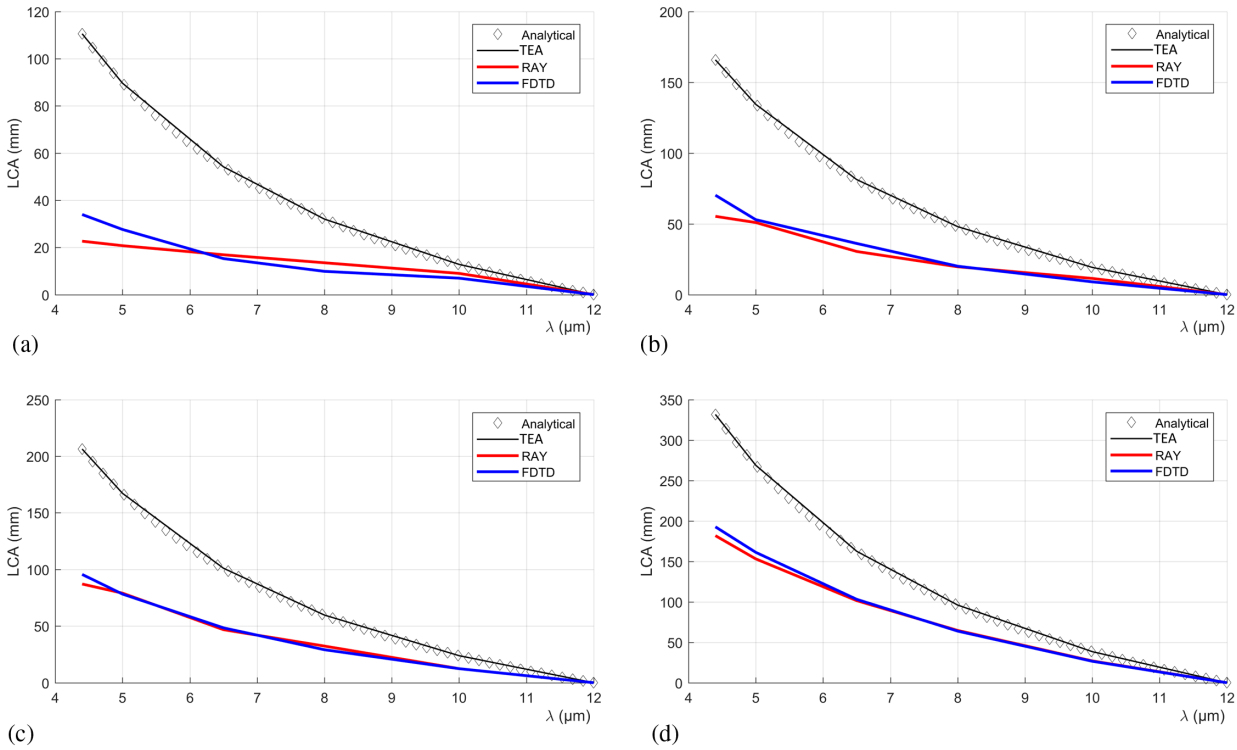

Fig. 10. LCA for a ZnS-air-IRG25 MLDOE for various $F/\#$: (a) F/10, (b) F/15, (c) F/20, and (d) F/30. The "best" focal plane is defined as the plane $z > 0$ with highest Strehl ratio. The TEA model, ray model, and FDTD are, respectively, displayed in black, red, and blue. The analytical LCA is displayed with black diamonds [Eq. (4)]. FDTD is the reference curve.

Table 1. Table Displaying the RMSE Values between the Ray Model and FDTD (Reference) for the Two Studied MLDOE Designs[a]

		LCA			
RMSE	**Strehl Ratio**	**F/10**	**F/15**	**F/20**	**F/30**
ZnS–Air–IRG25	16.1 %	5.7 mm	6.5 mm	3.8 mm	5.6 mm
ZnS–Air–Ge	15.3 %	5.8 mm	7.5 mm	6.6 mm	4.2 mm

[a]The numerical values are based on the 10 subfigures displayed in Figs. 8–10.

RMSE is 15%, relative to the extent of the considered physical quantity (Strehl ratio, LCA). This means, at least in the two MLDOE cases studied in this paper, that the ray model is not suited for the accurate determination of optical metrics and must be complemented by rigorous calculations, such as FDTD. In the meantime, as shown in Figs. 8–10, the ray model is able to accurately model the evolution of the Strehl ratio and LCA for multiple f-numbers, wavelengths, and MLDOE combination materials, which is not at all the case for the TEA model.

6. CONCLUSION

We have shown that our ray model is more accurate than the TEA model for f-numbers between 10 and 30, at least for the two presented MLDOE designs. The TEA model matches the asymptotic behavior of the ray model for very high f-numbers (Fig. 8). The latter allows us to extend the scalar theory to low f-numbers and high aspect ratios. Because of its scalar nature, the ray model is fast to compute and can even be used for off-axis MLDOE simulations. This makes it valuable because three-dimensional FDTD simulation takes a huge amount of processing time and requires complex three-dimensional MLDOE layouts. Particularly when multiple wavelengths, materials, and f-numbers are studied (e.g., chromatic aberration estimation), the FDTD time requirements become difficult to handle. Therefore, if FDTD is necessary for verification purposes, the ray model examined here should be used as an optimization and estimation tool.

In addition, in the two cases studied here, the ray model provides pessimistic results compared with FDTD, which, in the context of predicting MLDOE performance with an approximate model, is a major advantage. Thereby, the ray model provides a form of image quality insurance, being a worst-case scenario, at least in the two cases studied here. This is due to a higher number of "operating" zones for FDTD than for the ray model, leading to increased peak intensity at the focal point. Physically, interference inside the MLDOE leads to a converging wavefront for the intermediate zones, where the aspect ratio is sufficiently high to block geometrical rays (total internal reflection). Therefore, the ray model provides pessimistic estimations because it neglects the wave nature of light propagating inside the MLDOE.

In contrast to the TEA model, the ray model is able to compute an average transmission and to take into account total internal reflection. These quantities can be used as additional metrics to evaluate the performance of MLDOE design without requiring Fourier optics wave propagation. The ray model examined here is, therefore, a powerful designing tool when

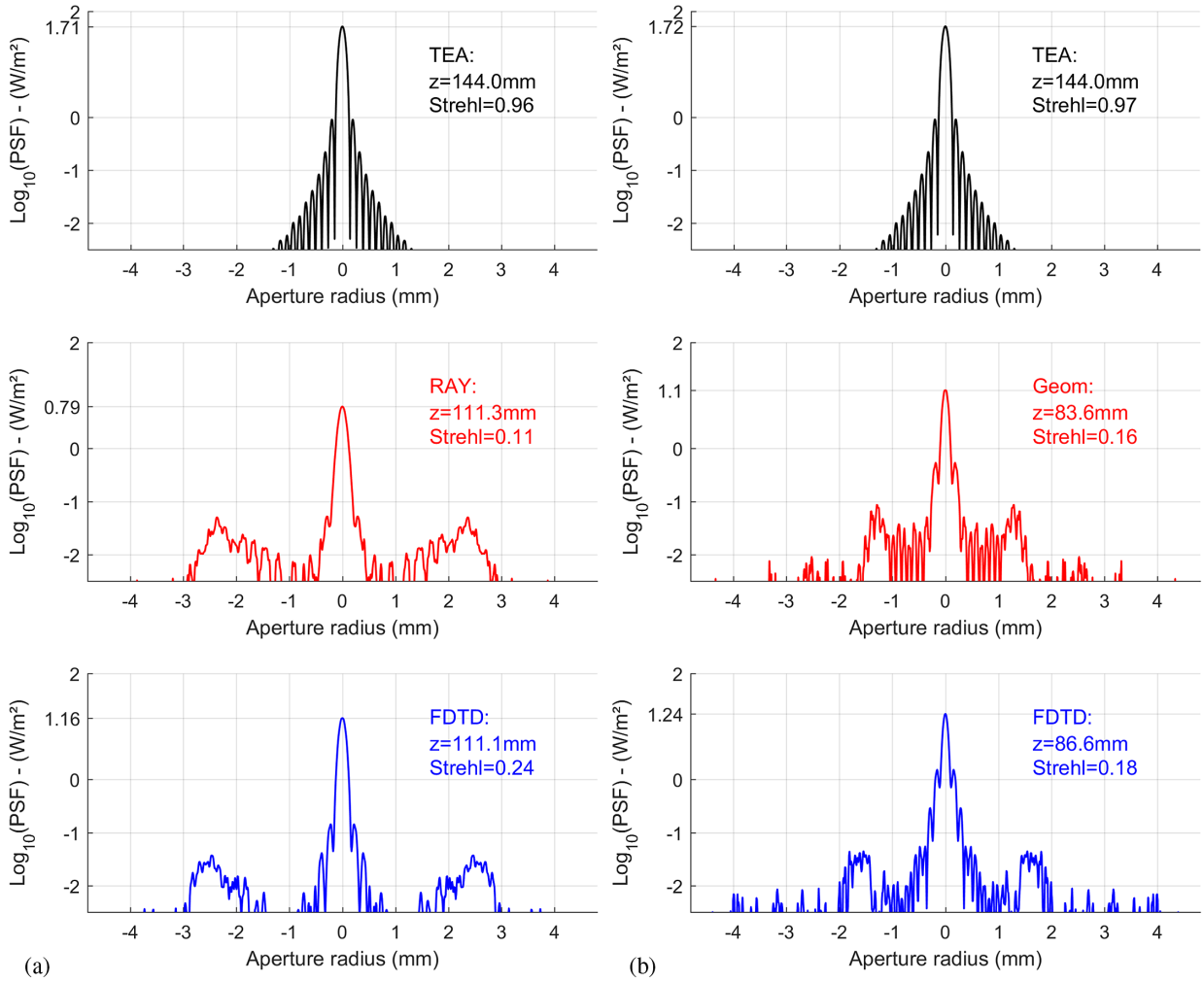

Fig. 11. One-dimensional cut of the logarithm of the PSF, at the best focus, for the two F/15 MLDOE designs: (a) ZnS-air-Ge, (b) ZnS-air-IRG25. The TEA model, ray model, and FDTD are, respectively, displayed in black, red, and blue. In both (a) and (b), the TEA model provides purely diffraction-limited PSF. In contrast, the ray model and FDTD both predict a very different PSF shape, with a clear secondary ring of light and a weaker central lobe. Contrary to the TEA model prediction, the PSF shape strongly depends on the MLDOE design.

numerous materials, f-numbers, and wavelengths must be studied.

APPENDIX A

The LCA for the ZnS-air-IRG25 MLDOE is presented in Fig. 10, for various F-numbers: Similarly to Fig. 9, Fig. 10 demonstrates that the LCA does not follow the analytical curve as expected by the TEA model.

A one-dimensional cut of the irradiance at the best focal plane for both MLDOE designs (corresponding to the yellow lines in Figs. 6 and 7) is displayed in Fig 11: The irradiance pattern predicted by the ray model and FDTD differ from the TEA approach, for the two MLDOE designs.

Disclosures. The authors declare no conflicts of interest.

Data availability. No data were generated or analyzed in the presented research.

REFERENCES

1. J. A. Sobrino, F. Del Frate, M. Drusch, J. C. Jimenez-Munoz, P. Manunta, and A. Regan, "Review of thermal infrared applications and requirements for future high-resolution sensors," IEEE Trans. Geosci. Remote Sens. **54**, 2963–2972 (2016).
2. M. Shimoni, "Feasibility study on hyperspectral thermal-infrared sensor," in *GSP Research* (ESA, 2005).
3. SCHOTT, "Reliable solutions for the infrared industry," 2020, https://www.schott.com/advanced_optics/english/products/optical-materials/ir-materials/infrared-chalcogenide-glasses/index.html.
4. Y. Arieli, S. Noach, S. Ozeri, and N. Eisenberg, "Design of diffractive optical elements for multiple wavelengths," Appl. Opt. **37**, 6174–6177 (1998).
5. C. W. Sweeney and G. E. Sommargren, "Harmonic diffractive lenses," Appl. Opt. **34**, 2469–2475 (1995).
6. D. Faklis and G. M. Morris, "Spectral properties of multiorder diffractive lenses," Appl. Opt. **34**, 2462–2468 (1995).
7. C. Fan, Z. Wang, L. Lin, M. Zhang, and H. Fan, "Design of infrared telephoto-optical system with double layer harmonic diffractive element," Chin. Phys. Lett. **24** 1973–1976 (2007).
8. C. Xue, Q. Cui, T. Liu, Y. Liangliang, and B. Fei, "Optimal design of multilayer diffractive optical element for dual wavebands," Opt. Lett. **35**, 4157–4159 (2010).

9. S. Mao, Q. Cui, M. Piao, and L. Zhao, "High diffraction efficiency of three-layer diffractive optics designed for wide temperature range and large incident angle," Appl. Opt. **55**, 3549–3554 (2016).
10. B. Zhang, Q. Cui, and M. Piao, "Effect of substrate material selection on polychromatic integral diffraction efficiency for multilayer diffractive optics in oblique incident situation," Opt. Commun. **415**, 156–163 (2018).
11. D. A. Pommet, M. Moharam, and E. B. Grann, "Limits of scalar diffraction theory for diffractive phase elements," J. Opt. Soc. Am. **11**, 1827–1834 (1994).
12. G. Greisukh, G. Danilov, E. Ezhov, S. Stepanov, and B. Usievich, "Comparison of electromagnetic and scalar methods for evaluation of efficiency of diffractive lenses for wide spectral bandwidth," Opt. Commun. **338**, 54–57 (2015).
13. G. Greisukh, G. Danilov, S. Stepanov, A. Antonov, and B. Usievich, "Spectral and angular dependences of the efficiency of three-layer relief-phase diffraction elements of the IR range," Opt. Spectrosc. **125**, 964–970 (2018).
14. G. Greisukh, G. Danilov, S. Stepanov, A. Antonov, and B. Usievich, "Minimization of the total depth of internal saw-tooth reliefs of a two-layer relief-phase diffraction microstructure," Opt. Spectrosc. **124**, 98–102 (2018).
15. H. Yang, C. Xue, C. Li, and J. Wang, "Optimal design of multilayer diffractive optical elements with effective area method," Appl. Opt. **55**, 1675–1682 (2016).
16. C. Yang, H. Yang, C. Li, and C. Xue, "Optimization and analysis of infrared multilayer diffractive optical elements with finite feature sizes," Appl. Opt. **58**, 2589–2595 (2019).
17. F. Wyrowski and M. Kuhn, "Introduction to field tracing," J. Mod. Opt. **58**, 449–466 (2010).
18. H. Sauer, P. Chavel, and G. Erdei, "Diffractive optical elements in hybrid lenses: modeling and design by zone decomposition," Appl. Opt. **38**, 6482–6486 (1999).
19. A. Nemes-Czopf, D. Bercsényi, and G. Erdei, "Simulation of relief-type diffractive lenses in ZEMAX using parametric modelling and scalar diffraction," Appl. Opt. **58**, 8931–8942 (2019).
20. V. Laborde, J. Loicq, and S. Habraken, "Modeling infrared behavior of multilayer diffractive optical elements using Fourier optics," Appl. Opt. **60**, 2037–2045 (2021).
21. J. W. Goodman, "The angular spectrum of plane waves," in *Introduction to Fourier Optics* (McGraw-Hill, 1996), Chap. 3.
22. K. Matsushima and T. Shimobaba, "Band-limited angular spectrum method for numerical simulation of free-space propagation in far and near fields," Opt. Express **17**, 1967–19662 (2009).
23. B. R. Org, "ASAP NextGen," 2022, https://breault.com/asap/.
24. Optiwave Photonic Software, "OptiFDTD Overview," 2022, https://optiwave.com/optifdtd-overview/.